Distributed Drift Chamber Design for Rare Particle Detection in Relativistic Heavy Ion Collisions

R. Bellwied[a], M.J. Bennett[b], V. Bernardo[c] H. Caines[d], W. Christie[e], S. Costa[f], H.J. Crawford[b], M. Cronqvist[b], R. Debbe[e], R Dinnwiddie[g], J. Engelage[b], I. Flores[b], R. Fuzesy[g], L. Greiner[b], T. Hallman[e], G. Hoffmann[h], H.Z. Huang[i], P. Jensen[h], E.G. Judd[b], K. Kainz[j], M. Kaplan[k], S. Kelly[i], P.J. Lindstrom[g], W.J. Llope[j], G. LoCurto[d], R. Longacre[e], Z. Milosevich[k], J.T. Mitchell[e], J.W. Mitchell[l], E. Mogavero[e], G. Mutchler[j], S. Paganis[h], E. Platner[j], R. Potenza[f], F. Rotondo[c], D. Russ[k], I. Sakrejda[g], A. Saulys[e], J. Schambach[h], J. Sheen[a], N. Smirnoff[c], C. Stokeley[j], J. Tang[h], A.L. Trattner[b], S. Trentalange[i], G. Visser[b], J.P. Whitfield[k], F. Witharm[g], R. Witharm[g], and M. Wright[j]

[a]Wayne State University, Detroit, MI 48201

[b]Space Science Laboratories, University of California, Berkeley, California 94720

[c]Yale University, New Haven, CT 06520

[d]Ohio State University, Columbus, Ohio 43210

[e]Brookhaven National Laboratory, Upton, New York 11973

[f]Universitá di Catania and INFN-Sezione di Catania, I-95129 Catania, Italy

[g]Lawrence Berkeley National Laboratory, Berkeley, CA 94720

[h]University of Texas, Austin, Texas 78712

[i]University of California, Los Angeles, California 90095

[j]Rice University, Houston, TX 77251

[k]Carnegie Mellon University, Pittsburgh, PA 15213

[l]NASA Goddard Space flight Center, Greenbelt, Maryland 20771

This report describes a multi-plane drift chamber that was designed and constructed to function as a topological detector for the BNL AGS E896 rare particle experiment. The chamber was optimized for good spatial resolution, two track separation, and a high uniform efficiency while operating in a 1.6 Tesla magnetic field and subjected to long term exposure from a 11.6 GeV/nucleon beam of 10^6 Au ions per second.

1. Introduction

In 1977, Jaffe predicted the existence of the H_0, a six-quark ($uuddss$) state bound with respect to strong decay[1]. Subsequent work by Donoghue *et al.* placed a weak decay lifetime for the H_0 in the neighborhood of $2-6\times10^{-9}s$[2]. The possibility of this long lifetime, coupled with the copious production of Lambda hyperons (uds) observed in heavy ion collisions[3], led Baltz *et al.* to predict a large production of $\Lambda\Lambda$ states in relativistic heavy ion collisions[4]. Assuming that the H_0 has a substantial overlap with the $\Lambda\Lambda$ state, heavy ion collisions should create a favorable environment for observing this uncharged exotic state.

The E896 experiment[5] was proposed to search

for H_0 production in relativistic $Au + Au$ collisions at the Brookhaven National Laboratory (BNL) AGS. The experiment was designed to be sensitive to weak decay channels of neutral particles, and specifically optimized to detect the $H_0 \rightarrow \Sigma^- + p$ decay channel. The main components of the experimental setup were two topological tracking detectors, shown in Figure 1. One, a 15 plane silicon drift detector array, has been reported in a previous paper[6]. The other is a distributed drift chamber (DDC), located in a 1.6 Tesla analyzing magnet with a 6.2 Tesla sweeping magnet and collimator placed just upstream to minimize charged particles reaching the DDC. In the present paper, we discuss the design and implementation of the DDC.

2. Design

2.1. Designing the Tracking Detector

The primary constraints placed on the tracking detector in the E896 experiment were that it unambiguously identify the topological signature of particle decays, provide enough track information to reconstruct the rigidity of each charged daughter produced, and operate at high rates in a high flux environment. Given these restrictions, a distributed drift chamber (DDC) was the optimal detector for this experiment. A Multiwire Proportional Chamber would lack the spatial resolution (approximately an order of magnitude less than a drift chamber) necessary to reconstruct the invariant mass of the $\Sigma^- + p$ channel and thereby distinguish it from the $K^- + p$ background produced in $n + n$ interactions. A Time Projection Chamber approach was not chosen due to insufficient double track resolution and because typical recovery rates are much slower than that of a drift chamber. A Drift Tube configuration was rejected because its mass is an order of magnitude larger than a DDC, as well as the fact that its assembly would be significantly more difficult.

For the physical size of the tracking detector, most of the outer dimensions were constrained by the bore of the 48D48 Analyzing Magnet. The 48D48 was chosen because it provides the largest fiducial volume of any of the standard BNL magnets with a strong enough magnetic field to allow identification of the daughter particles. The tracking detector (including electronics, cabling, etc.) is thereby constrained to be not more than $45cm$ in height, $120cm$ in width, and $120cm$ in depth. The inner or "working" area of the tracking detector was determined by a combination of the hardware constraints imposed by the Sweeping Magnet[7] and the simulations performed using GEANT[8]. The inner height of $20cm$ is a compromise between maximizing the available tracking volume and allocating finite space for structural integrity and the necessary on-board electronics.

To reduce the number of neutral and charged particles interacting with the DDC structure, a $50cm$ long lead-tungsten collimator was designed and placed $40cm$ downstream of the target. A vertical opening angle of $2.7°$ was determined by GEANT simulations to be optimum for the system, effectively cutting the vertical acceptance of the DDC, $132cm$ downstream of the target, in half. The maximum inner width of the tracking detector was determined by the background Monte Carlo. The results indicated that the central area of the chamber should be instrumented to detect the H_0 decays, while the area containing the beam and lower rigidity positively charged beam fragments must remain sparce to reduce secondary interactions. Additionally, the low rigidity area on the negative bend side should also remain empty to reduce the background of π^- particles produced in the $Au + Au$ collisions. Accordingly, the collimator was completely open in the X direction to beam right. To beam left the opening angle is drawn from the target pointing to the last beam left active wire in the most upstream part of the DDC. The chamber and magnets were oriented $-3.2°$ from the $0°$ beamline to maximize the acceptance around the mid-line for neutral particles produced in the target and to resolve charged daughter particles produced by their decays.

In the active area of the DDC a minimum of $2mm$ cell radius was required to produce enough primary electrons liberated by the passage of a minimum ionizing particle to be detectable. Simulations determined this was sufficient granularity transverse to the direction of the magnetic field to

resolve the two particles in the $\Sigma^- + p$ channel. The required granularity along the beam direction (Z) was determined to be $\sim 0.5cm$. This is a compromise among the need for multiple measurements along the Σ^- track, the need to maximize the depth of the detector to increase the number of H_0 decays observed, and the spatial constraints of onboard electronics used to outfit the instrument.

2.2. Cell Configuration

The internal cell configuration was optimized by performing extensive simulations using GARFIELD[9]. The configurations which achieved the best spatial resolution were the ones in which the ratio of the cell width to depth was maximized. Since the cell radius is set to $2mm$, based on two track separation and mechanical considerations the only option in maximizing the width to depth ratio was to minimize the cell depth. The cell half-depth was set at $3mm$, which is the minimum thickness having sufficient strength to support and maintain tension for the combination of anode and field shaping wires in the sense planes ($\sim 5kg$). GARFIELD simulations were run producing plots of lines of equipotential, in the presence of no magnetic field (Figure 2a), drift lines in the presence of a 1.6T field (Figure 2b), and drift distance versus time. The $4mm \times 6mm$ cell showed a "bleed" over of drift electrons to neighboring wires for only about 20% of the outer most tracks. An in depth comparison of these results to actual data will be discussed in the following section. The $2mm$ cell radius restriction was relaxed for the downstream half of the chamber where a larger cell size ($8mm \times 8mm$) was used in this area where expanded coverage was more critical than double track resolution[1].

Three different sense wire orientations, $0°(X)$, $+15°(T)$, and $-15°(U)$ were chosen to obtain the required stereoscopic projection to allow momentum reconstruction. The T and U orientations were determined using tracking reconstruction of Monte Carlo data to maximize the P_y resolution while minimizing the confusion caused when multiple particles impact the same wire. Similarly, track reconstruction with momentum analysis was used to optimize the final plane sequencing, $XX'UU'XX'XX'TT'XX'$ (primes designate planes with cells shifted by half a cell's width with respect to an unprimed plane).

2.3. Internal Construction

Once the overall size, shape, and type of tracking detector had been fixed, the construction materials and the internal configuration were determined. The field shaping cathode planes were constructed with conducting foils rather than wires due to the field problems that arise in transitioning between sense wires with different orientations. The use of foils places stringent requirements on the flatness and spacing uniformity of the NEMA G10 cathode mounting frames. We were able to hold individual frame tolerances to less than $\pm 15\mu m$ over a 1 meter distance. G10 was chosen for both its structural strength and electronic insulating properties. Further, cryogenic grade G10 was chosen to avoid any problems with boron contaminants which are known to bind with free electrons and cause a loss of signal. A carbon impregnated foil used in EMP (Electromagnetic pulse) technology was chosen over the more common aluminized or silver deposited mylar due to its bulk conductive properties. These allowed a single foil to be shared between 2 sense planes to provide the shaping potential. The bulk conductive properties also reduced the chance of charge build up and subsequent discharge to the sense wires. To avoid electric field problems being induced by foil edges (e.g. break down, polymerization of wires, etc.), the foils were stretched across the entire width and breadth of the G10 frames. This meant extending them into both the π^- and beam regions.

The potential for beam-foil interactions was reduced by removing a $3cm$ diameter area from each foil centered along the expected beam trajectory. To avoid electric field anomalies at the edges of the active region the sense wires were bounded with a final cell containing a larger diameter terminating wire tied directly to ground. To obtain the amplification required by the front end elec-

[1]This decision is based on an assumed H_0 lifetime of between $4cm$ and $100cm$ $c\tau$ for which the majority of the H_0 decays in the DDC occur in the upstream half of the chamber

tronics (FEE) and to avoid avalanche problems, $20\mu m$ diameter gold-plated tungsten wire was chosen for the sense wires. The tensile strength of tungsten allows for the smallest diameter wire, hence greatest electric fields with lower voltages. The gold plating provides a smoothness which makes for a more uniform field over the length of the wire. It also allows the wires to be soldered. The terminating anode wire on either end of the sense planes is 75 micron beryllium-copper with a 5% gold strike, the same as the cathode wires used for shaping the field around each anode(sense) wire.

The use of foils also required special attention to eliminate any gas flow restrictions which might create pockets in the chamber which would lead to anomalous drift characteristics. One centimeter diameter holes were placed in alternate corners of each foil and 8 hour purges were required after any opening of the chamber. This design was sufficient to guarantee uniformity in the drift properties. The stability of the drift properties of the gas was monitored during the experiment by connecting the DDC gas output to a single wire TPC containing an internal ^{106}Ru source, the so-called canary.

2.4. Constraints on Drift Gas

Although the portion of the chamber where beam and projectile fragments pass is not active, it still contains chamber gas. Thus it is preferable to use a Helium-based gas to reduce the number of delta rays and secondary interactions produced in the gas by the primary beam and projectile fragments. A 50%:50% mix of helium (He) and ethane (C_2H_6) bubbled though methyl alcohol was chosen. The introduction of 1-5% methyl alcohol is known to reduce polymerization of wires, or "aging", in drift chambers[10]. An additional reason for using a helium based gas is that the drift velocity is less sensitive to the magnetic field than in an argon based gas[11]. The effect of the magnetic field on pulse height is also reduced[12]. The gas mixture flowed continuously through the DDC at a pressure slightly above atmospheric.

2.5. Mechanical Construction

All wires are epoxied to the G10 frames to maintain their tension, then soldered to internal artwork etched onto the frames. Twelve sense ($XX'UU'XX'XX'TT'XX'$) and twelve foil planes, each outfitted with a 30 durometer butylene O-ring, are bound together with 316-SS (Stainless Steel) posts and flathead binder screws to form a single module, shown in Figure 3. The planes were indexed to each other using 3 anodized pins for an interplane wire accuracy of $\sim 10\mu m$. These pins also facilitated indexing neighboring modules to within an accuracy of $\sim 40\mu m$. The survey of the entire DDC with respect to other elements in the experiment was completed with an accuracy of $\sim 70\mu m$. The modules are 7.2 and $9.6cm$ deep for the $6mm$ deep cells and $8mm$ deep cells, respectively. The $6mm$ modules had 64 sense wires per plane and the $8mm$ modules had 46. The foil planes between UU' and TT' sense planes were constructed by replacing the G10 frame with a pre-stressed 316-SS frame laminated with kapton artwork. The two stainless frames created a bridge structure for each module to maintain wire tension and module alignment.

Each module is equipped with a pillow block assembly on each of its lower corners to allow mounting to a rail system. The rigidity and alignment of the complete DDC is accomplished by binding the 12 modules[2] between a $1.27cm$ aluminum frame and an aluminum "strongback", composed of a similar $1.27cm$ aluminum frame and $7.5cm$ box beam. Twenty-four (24) one meter long threaded rods brought the assembly together to form a gas-tight volume. Both the frames and strongback were ground flat to $15\mu m$ and outfitted with two gold-plated mylar windows each. Gas was exhausted through the region between the windows on either frame thus functioning as a buffer to prevent moisture from entering the active region of the chamber and to avoid changing the He to C_2H_6 ratio in the active region near the windows. The assembled DDC was mounted on the rail system to enable it to slide into the 48D48

[2]For a total of 144 planes (i.e. six $6mm$ modules and six $8mm$ modules).

magnet when outfitted with cable trays, nitrogen cooling ducts, and cabled with 34pin twist-n-flat cables as shown in Figure 4.

3. Electronics

3.1. HV distribution

A $1mm$ connector was embedded into the edge of each frame and soldered to the internal artwork to allow for a high voltage (HV) connection. Two channels of a LeCroy 1440N HV supply were assigned to each module. Each of these 1440N channels supplied a HV Bus card, containing 12 mating connectors, which distributed HV to an entire module's foil or sense planes. The HV bus card routed the 1440N HV to each connector via a field effect transistor (FET). A power distribution panel for the FETs was constructed to allow disabling HV to individual planes of the DDC as required. A Labview interface was developed to monitor and control the high voltage system.

3.2. Front End Cards

Constraints placed on the electronics for this detector were as stringent as the mechanical requirements. Specifically, the front end electronics (FEE) required short shaping time for good double pulse resolution, low power because of the large number of channels and restricted space, high channel density, and low operational threshold. Due to these restrictions, the experiment chose to develop a custom FEE board that utilized the ASD8 chip already in use by PHENIX at RHIC[13]. The ASD-8 is an 8 channel amplifier, shaper, and discriminator integrated circuit, constructed in an npn bipolar process for low noise, high speed, and high gain power efficiency. It provides a low operational threshold ($\sim 1fC$), suitable shaping time ($\sim 5ns$), and good double pulse resolution ($\sim 20ns$), all with low power consumption ($\sim 15mW/chnl$). Even with this low power consumption is was necessary to flow cold nitrogen gas over the FEE cards to keep their temperature below 50°C.

The FEE card was designed to service 16 sense wires. As such the card contained two ASD8's, each consisting of 8 identical ASD channels with differential inputs and outputs. Since the low threshold readout is susceptible to interference pickup, the FEE cards were mounted directly on the chamber. One side of the differential input was connected via a copper trace masked on the G10 frame to a sense wire while its differential was connected to a companion trace which was left un-terminated. The FEE cards were mounted on the top of the chamber, each bolted with a solid ground connection to a silver plated brass ground plate which covered the entire top surface of the G10 frames. The signal connectors, edge mounted on the G10 frames, protruded through slots in this ground plate to connect to the FEE cards.

3.3. Readout

Another desirable feature of the ASD8 chip was that its differential output was compatible with the ECL input required by the LeCroy 1879 fastbus TDCs used in the experiment. The 96 channel pipeline TDC was chosen for its high density and speed. The $2ns$ resolution set construction tolerances for the DDC at $\pm 70\mu m$. The size of the 1879 readout buffer was reduced to increase data collection speed and still maintain multihit capability in the useful time range. The LRS 1810 Clock and Trigger (CAT) module was used to provide the calibration and common stop trigger signals to the 1879s. Event readout of the four fastbus crates into an LRS 1190 VME memory module was via LRS 1821 segment managers.

4. Calibration

Approximately 1.2×10^8 events were recorded from 11.6A GeV/c $Au + Au$ collisions using the DDC during a 4 week period in April of 1998. A second run, which produced 6×10^6 events using a beam of 12GeV/c protons on a Be target, was staged in September of 1998. Data from both these runs were used to calibrate and characterize the DDC as discussed in the following sections.[14]

5. Time Calibration

Time calibration of the system was accomplished by pulsing either the FEE cards or the HV foils and issuing a subsequent stop pulse to

the TDCs via the CAT module after a set period of time. An Ortec 462 Time Calibrator with an accuracy of $50ps$ was utilized for this procedure. The calibration pulse was input to the HV distribution cards discussed above which served to distribute the time calibration pulses to the HV foils and isolate the Ortec 462 unit from the LRS 1440 HV supply powering the foils.

The TDC offsets were determined on a per run basis for each TDC channel. To determine the offset for a particular channel, the TDC values were histogrammed for a sample of events and the resulting spectrum was subject to an edge finding algorithm. The edge finding algorithm involved fitting a half-gaussian to the leading edges of the TDC spectra and then calculating the TDC value that corresponded to half the maximum value of the gaussian.

In order to flag sections of the DDC that suffered from very low efficiency or noisy electronics, software was developed to generate a "kill file" on a per run basis. For each wire in the DDC the hit occupancy, mean TDC value and rms TDC value were determined for each run. Wires for which these summary statistics did not fall within a particular range were written to a kill file. The kill file was subsequently read in by the tracking software and the wires therein were not used to constrain tracks. The use of the kill file improved the momentum resolution by eliminating noisy wires and increased the track finding efficiency by decreasing the number of instances that the finding software incorrectly located a track's endpoint within a dead section.

5.1. Drift Curve Calibration

The determination of the correlation between the local parameters of a track crossing a drift cell and the measured drift time is an essential calibration for drift chamber detectors. The presence of a magnetic field introduces a velocity-dependent term from the Lorentz force equation and thus complicates the drift behavior of the ionization electrons. The elliptical and circular lines shown in Figure 2 are lines of constant drift time or isochrones. In the absence of magnetic field effects, these lines are concentric circles centered at the location of the sense wire. The magnetic field distorts the geometry of the drift cell and renders the lines of constant drift time furthest from the sense wire elliptical in shape. This effectively introduces an angular dependence in the correlation between the distance of closest approach (between a charged track and the sense wire) and the measured drift time. In the case in which there is no magnetic field, the locus of points corresponding to a fixed distance of closest approach corresponds exactly to a circular isochrone, hence there is no angular dependence. In the presence of a magnetic field, the relevant isochrone is dependent on both the distance of closest approach and the angle at which the charged track crosses the drift cell.

5.2. Garfield

Garfield[9] is a computer program for the simulation of two and three dimensional drift chambers. The program exactly solves electrostatics in two dimensions using conformal mapping techniques. It also models diffusion, particle drift, avalanches and signal generation. The program can be used to generate field maps and drift time to drift distance correlations. The parameters chosen to describe the correlation between a track crossing and measured drift time were the distance of closest approach and the angle the bend plane track tangent made with the cave X axis. Garfield was used in an initial simulation of the characteristics of the DDC drift cells. A goal of this simulation was the determination of the relative importance of the distortions due to the presence of a large magnetic field. Figure 5 shows the Garfield generated correlation between t (the measured drift time) and R (the distance of closest approach between the track segment and the sense wire) for three different values of the angle ϕ. The Garfield simulation indicated that the deviations between drift curves of differing angle were greater than $2ns$ (the resolution of the 1879 TDCs) over 60% of the drift cell.

5.3. Measured Drift Correlations

The actual drift correlations were determined using a sample of rigid protons from the September 1998 proton run. Tracks were initially fit using the Garfield-based approximation to the true

drift correlations. The best fit track parameters were then extrapolated to each active detector cell and the distance of closest approach was plotted versus the measured TDC values in bins of the angular variable ϕ. The resulting drift correlations were parameterized and then used as input for subsequent iterations. The process was repeated until variations in the parameterization were of the same order as the detector resolution. Figure 6 shows a family of drift correlations as determined by this method, taken from the final iteration for the $8mm$ drift cells. As anticipated, deviations due to angular effects are visible at a level comparable to the resolution of the detector for $R > 0.3cm$.

5.4. Parameterization of Drift Correlations

The DDC drift correlations were parameterized using C^1 continuous splines. The requirement of continuous derivatives across break points was necessary because, as will be described later, the measurement error associated with a given value of R was taken to be proportional to the slope of the drift curve. Therefore discontinuities in the derivatives would translate into discontinuities in the χ^2 minimization algorithm. The parameterization used is shown in Equation 1.

$$\begin{aligned} t_1(0 < R <= b_1) &= p_1 + p_2 R + p_3 R^2 \\ t_2(b_1 < R <= b_2) &= t_1(b_1) + t_1'(R - b_1) \\ &+ p_3 \cdot (R - b_1)^2 + p_4 \cdot (R - b_1)^3 \\ t_3(R > b_2) &= t_2(b_2) + t_2'(R - b_2) \\ &+ p_5 \cdot (R - b_2) \end{aligned} \quad (1)$$

where t_1' and t_2' equal dt_1/dR and dt_2/dR respectively. The values of the parameters were derived via a maximum likelihood fit to the data. The break points were adjusted manually. The data were divided into angular bins and the fit parameters determined for each bin. For ϕ values inside the angular range of the fits linear interpolation between the two nearest drift curves was used. For values outside this range the closest drift curve was used. Table I shows the fit parameters and break points for the various angular bins.

5.5. Characterization of DDC Errors

Despite the presence of the sweeper magnet, the charged track background in the DDC made χ^2 increment based outlier rejection necessary. This is accomplished by initially constraining the track with all the hits associated by the pattern recognition software. Then, if the χ^2 increment contributed by a given hit is more than a user defined threshold, the hit is rejected. Rejected hits are typically associated with charged tracks other than the one being fit, or with noisy DDC electronics. The definition of the χ^2 increment is given as:

$$\chi^2_{inc} = [(t_m - t_p)/\sigma_t]^2 \quad (2)$$

where t_m and t_p are the measured and predicted drift time respectively, and σ_t is the statistical error.

The non-linear correlation between drift time and distance of closest approach implies the measured error also varies as a function of the cell local track parameters. Figure 7 shows the parameterized drift curves offset by $\pm 3\sigma$ errors, and superimposed upon measured drift correlations. In the Figure 7a, a constant error is used, in Figure 7b the error is parameterized as:

$$\sigma_t = \sigma_{TDC} + (dt/dR) * \sigma_{POS} \quad (3)$$

where σ_{TDC} and σ_{POS} are constants and dt/dR is the slope of the drift curve. It is clear that the constant error parameterization underestimates the error for large values of R, whereas the parameterization of Equation 3 more accurately reflects the actual errors. Consequently the latter was used in the track reconstruction.

5.6. Detector Resolution

The values of the constants were determined by requiring the pull statistic given by:

$$p = (t_m - t_p)/\sigma_t \quad (4)$$

be unbiased and of unit variance. Figure 8 shows the distribution of the pull statistic for the $6mm$ and $8mm$ drift cells. The parameters used are shown in Table II. The fact that the distribution of pull statistics is unbiased indicates that the

parameterization of the drift curves is not systematically biased. The unit variance of the pull distribution is required for p^2 to have a χ^2 distribution. As indicated in the table, the average position resolution for the cells was better than 160 microns.

5.7. Efficiency Calibration

The per plane efficiency was determined by reconstructing a sample of long straight tracks that left hits in the first and last modules of the DDC. The reconstructed track parameters were extrapolated to each detector plane and the nearest two sense wires were checked for a hit. The efficiency was defined as the ratio of hits to plane crossings. Wires that were killed because of low efficiency or noisy electronics were not used in the calculation of the efficiency. In other words, if a track intersected a plane in a killed region neither the hits nor crossing counter was incremented. Figure 9 shows the per plane efficiency averaged over a sample of runs from the late portion of the 1998 $AuAu$ run. The following systematic effects were observed:

1. The modules of $6mm$ deep cells were on average 7% less efficient that the modules with $8mm$ deep cells. This is to be expected due to the shorter track length in the $6mm$ cells and the correspondingly fewer primary drift electrons initially generated.

2. The planes that directly followed a stainless steel strong frame (T' and U') were systematically less efficient, because the higher capacitance on the signal lines in planes adjacent to these planes.

3. There was a systematic loss of efficiency observed in the first two modules of $6mm$ deep cells and the last module of 8mm deep cells.

4. The loss of efficiency observed in the last module of $8mm$ deep cells was correlated with the beam flux. At beam rates above 50K per AGS spill, the inefficiency in the rear of the chamber increased dramatically independent of target thickness.

6. Summary and Conclusions

A distributed drift chamber was built and used in a rare particle search at the BNL AGS. The design of the chamber was optimized for resolving V topologies while operating in a strong magnetic field and a high flux environment. The chamber met these design specifications, providing high quality data in a 11.6 A GeV/c beam of 10^8 Au ions per second. An example of a Λ decay in the drift chamber is shown in figure 10. The $He : C_2H_6$ gas used successfully minimized secondary interactions and multiple scattering in the chamber. Due to the presence of the strong magnetic field, the correlation between drift time and trajectory angle was found to play an important roll in correlation of time to distance. The overall chamber performance was not affected by the non-uniformity in the magnetic field of the analyzing magnet. The wires were positioned with sufficient accuracy ($10\mu m$) to achieve a single wire resolution of better than $160\mu m$ and plane efficiencies up to 97%. As designed and constructed, the DDC should be over 99% efficient in reconstructing the expected Σ^- tracks coming from an $H_0 \rightarrow \Sigma^- + p$.

7. Acknowledgements

We would like to express our thanks to the staff at Dinucci Corporation of Concord, CA and the Schaffer Grinding Company of Montibello, CA for the special attention paid to detail in the fabrication of mechanical components used in the construction of the DDC. We would also like to thank AGS beam operations crew for supplying us reliable beam and operating the beam channel during this experiment. Thanks are also due to the mechanical and electronics workshops at Lawrence Berkeley National Laboratory for help in the construction of the prototype drift chamber and much helpful advice. Finally, we would particularly like to recognize Gabriela Dinucci, Patrick Kelliher, and Dan Deboer for their assistance.

REFERENCES

1. R.L. Jaffe *Phys. Rev. Lett.* **V38** (1977) 195.

2. J.F. Donoghue, E.Golowich and B.R.Holstein, *Phys. Rev. D* **34** (1986) 3434.
3. A.C. Saulys et al., *HIPAGS'93*, MITLNS-2158 (93) 196. S.Ahmad et al., *Phys. Lett.* **B382** (96) 35.
4. A.J. Baltz et al., *Phys Lett.* **B325** (94) 7.
5. E896 proposal, Brookhaven National Laboratory AGS Program Advisory Committee, June 1993.
6. J. Takahashi et al., *NIM* **A439** (00) 497; J. Takahashi et al., *NIM* **A453** (00) 131.
7. A.J.Broadbent, *Brookhaven AGS E896 Split Pair Magnet Final Design Report*, Oxford Inst. Ltd. (96) 1.
8. I.M. Sakrejda et al. LBL-37384 (94) 125.
9. R. Veenhof, CERN Program Library **W5050** (93) 1.
10. J. Va'Vra, *NIM* **A252** (86) 547.
11. J. Va'Vra, *NIM* **A324** (93) 113.
12. U.J. Becker, *NIM* **A335** (93) 439.
13. F.M. Newcomer et al., *IEEE Trans. N.S.*, **V40** (1993) 630.
14. S. Kelly, Ph.D Thesis, Department of Physics, UCLA (2000), unpublished.

Table 2
Drift Chamber Resolution

Cell type	σ_{TDC}(ns)	$\sigma_{\mathrm{POS}}(\mu m)$
4mm	4.27	160
3mm	3.35	140

Table 1
Drift Curve Parameters

Cell	ϕ(rad)	p_1(ns)	p_2(ns/cm)	p_3(ns/cm^2)	p_4(ns/cm^3)	p_5(ns/cm)	b_1(cm)	b_2(cm)
4mm	0.0	1.82	107.21	568.14	3034.90	467.77	0.2	0.35
4mm	0.4	0.70	103.98	604.21	9207.20	10976.0	0.2	0.35
4mm	-0.4	0.35	170.67	927.06	-839.64	491.57	0.2	0.35
3mm	0.0	3.84	94.49	580.47	8009.4	3076.1	0.10	0.15
3mm	-0.4	2.08	139.77	397.80	-3118.9	678.27	0.1	0.15

Figure 1 Overview of the DDC system consisting of the target, sweeping magnet, collimator (black), DDC and Analyzing magnet. The Z-axis is rotated -3.2 degrees from the incoming beam to center the produced neutral particles (Λ) in the active part (shaded) of the DDC.
Figure 2a Garfield simulated trajectories of drifting electrons and the lines of equipotential for a single DDC cell with no magnetic field present. Note how none of the drift lines extend outside of the designated cell boundaries.
Figure 2b Garfield simulated trajectories of drifting electrons and the lines of equipotential for a single DDC cell in a 1.6 Tesla vertical B_y field. Note how many of the drift lines extend outside the designated cell boundaries and into the adjoining cells.
Figure 3 DDC modules are constructed by alternating 12 of the laminated sense planes in the proper order (xxttxxxxuuxx) with 12 HV foil planes.
Figure 4 The completed drift chamber with cables being inserted in the 48D48 analyzing magnet.
Figure 5 Garfield generated correlation between drift time t and distance of closest approach R, for three values of ϕ.
Figure 6 Measured drift correlations. Data were binned in ϕ, and the distance of closest approach (cm) versus measured drift time (ns) is plotted.
Figure 7a Parameterization of drift curve offset by $\pm 3\sigma$ errors. The errors were parameterized by $\sigma_t =$ constant.
Figure 7b Parameterization of drift curve offset by $\pm 3\sigma$ errors. The errors were parameterized by $\sigma_t = \sigma_{TDC} + (dt/dR)\sigma_{POS}$.
Figure 8 Pull distribution for a $4mm \times 6mm$ drift cell.
Figure 9 Bars represent the efficiency per module for the 1998 Au run. Efficiencies were obtained by averaging the per plane efficiency of the 12 planes in each module.
Figure 10 A Λ decay to pion and proton as found in a typical event from the $AuAu$ run. Note the clean neutral vertex and the low track background.

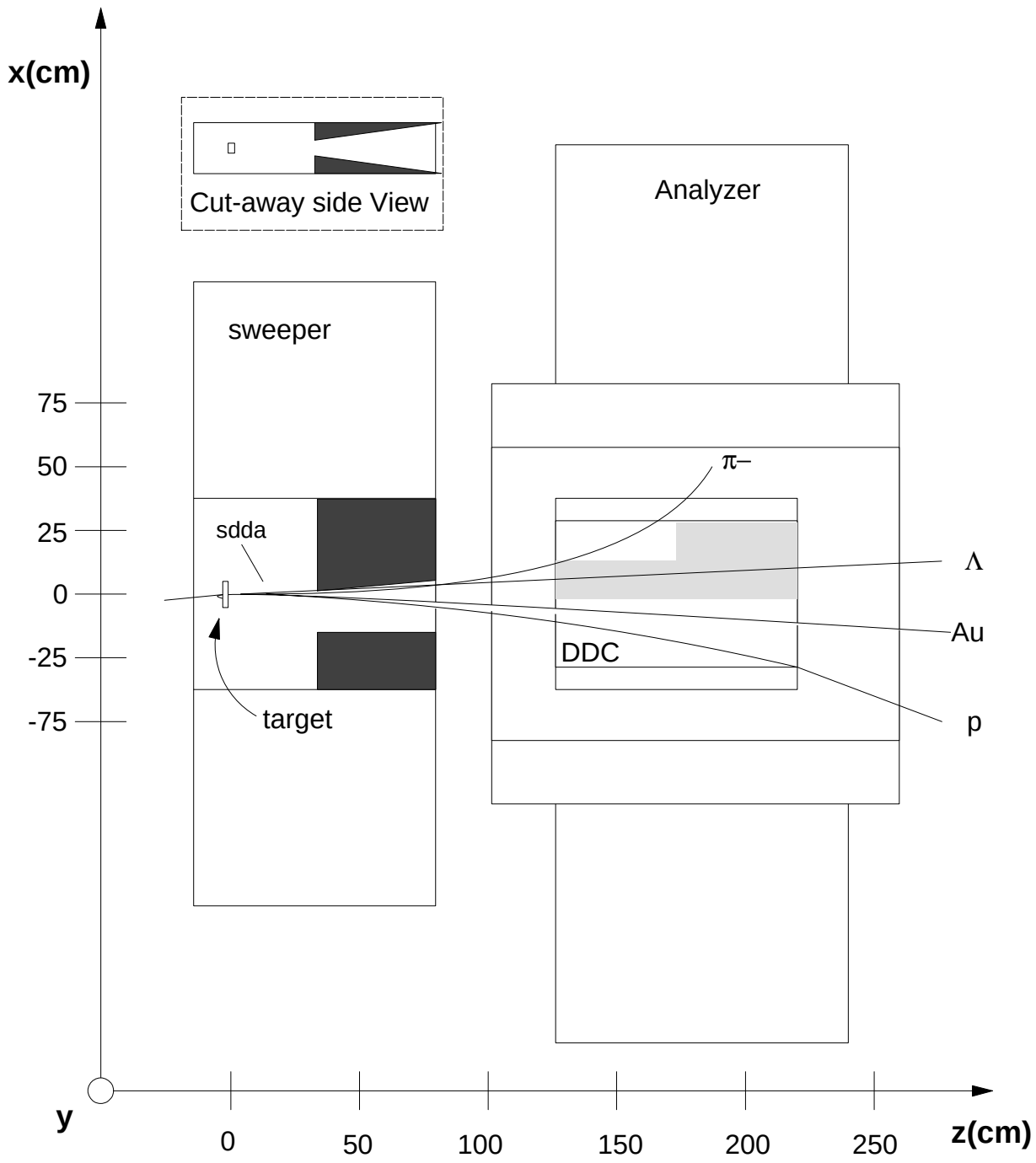
x(cm)
Cut-away side View
Analyzer
sweeper
75
50
25
0
-25
-75
sdda
π−
Λ
Au
DDC
p
target
y
0
50
100
150
200
250
z(cm)

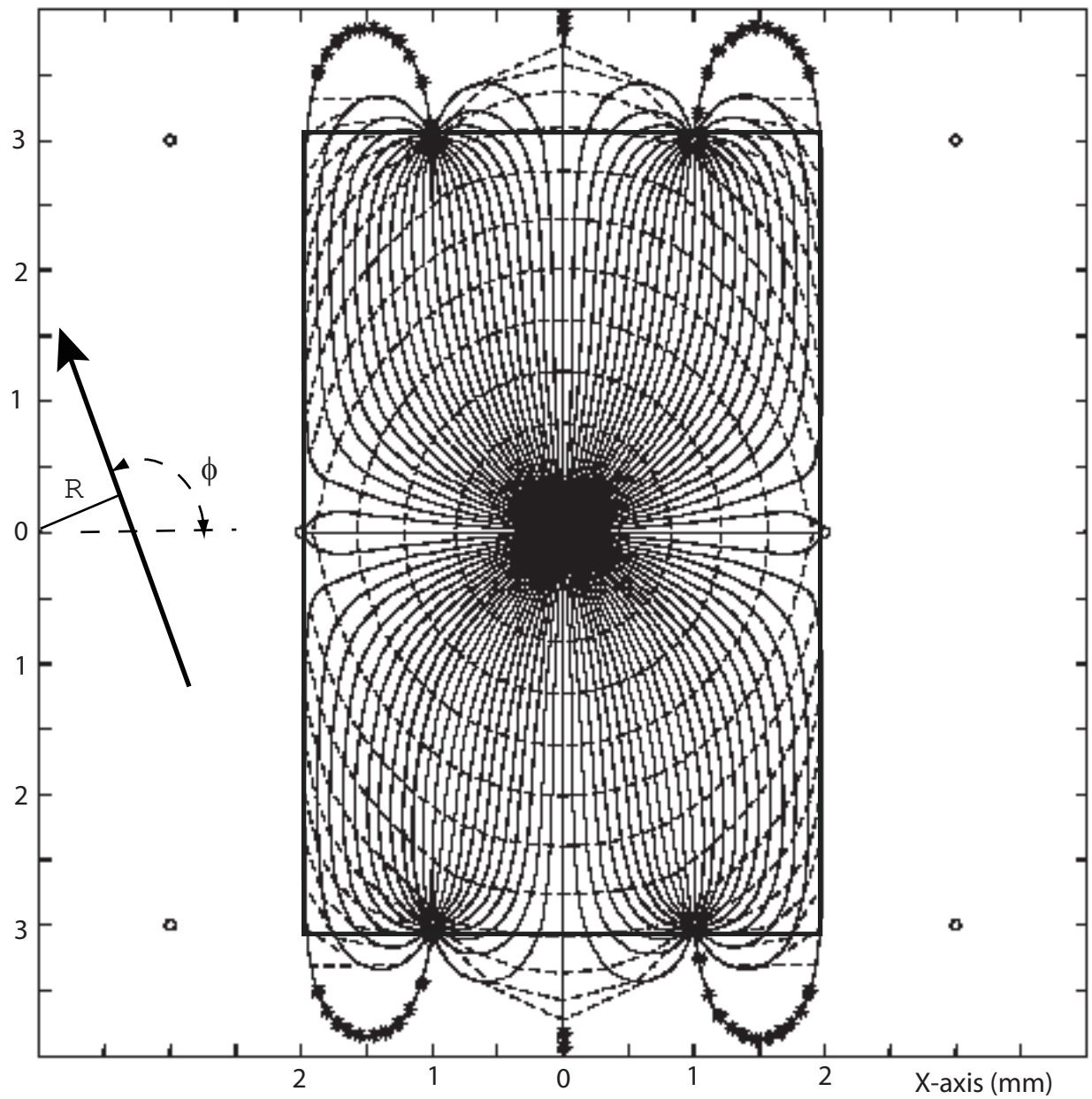
3
2
1
0
1
2
3
R
ϕ
2
1
0
1
2
X-axis (mm)

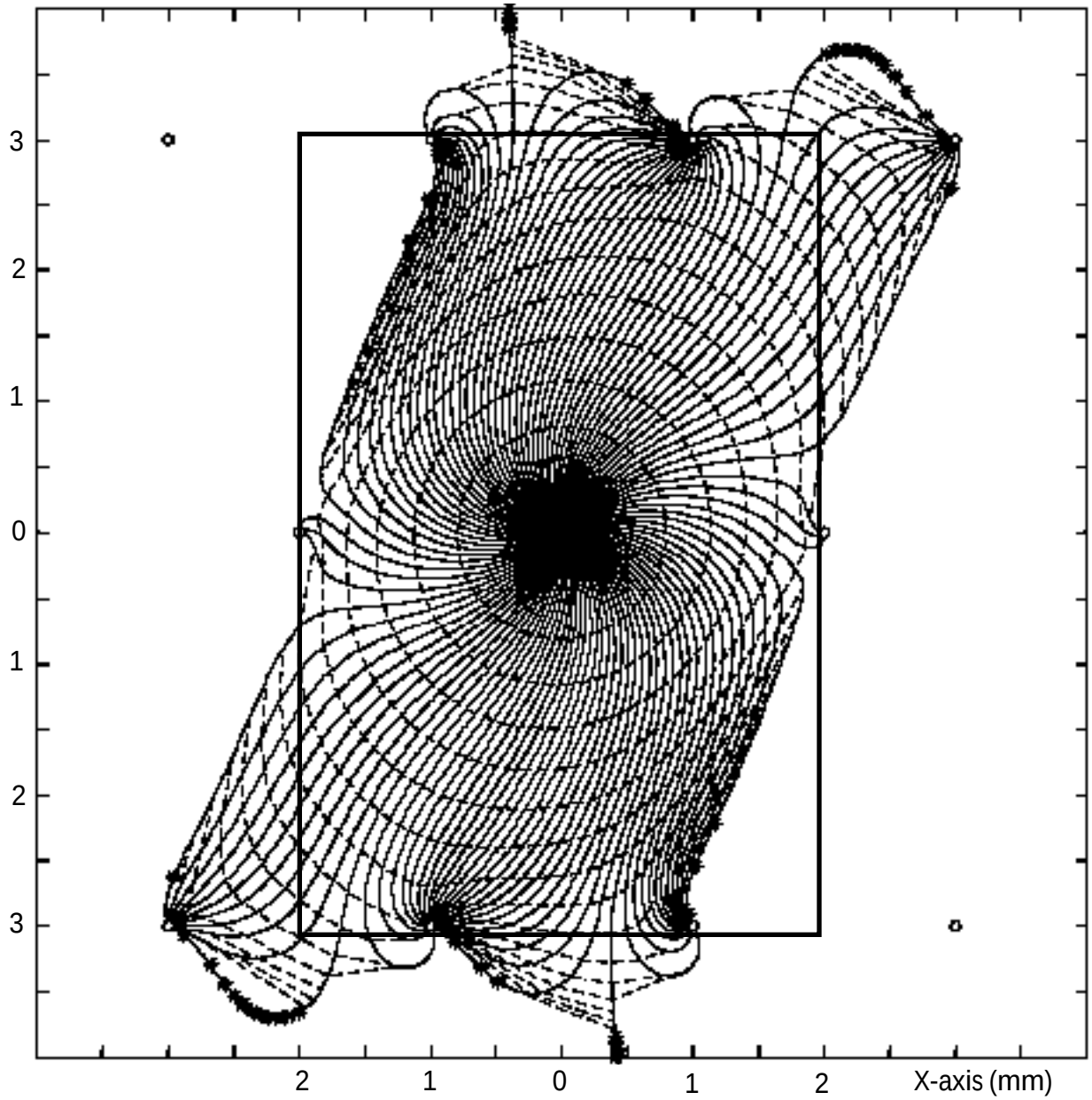
3
2
1
0
1
2
3
2
1
0
1
2
X-axis (mm)

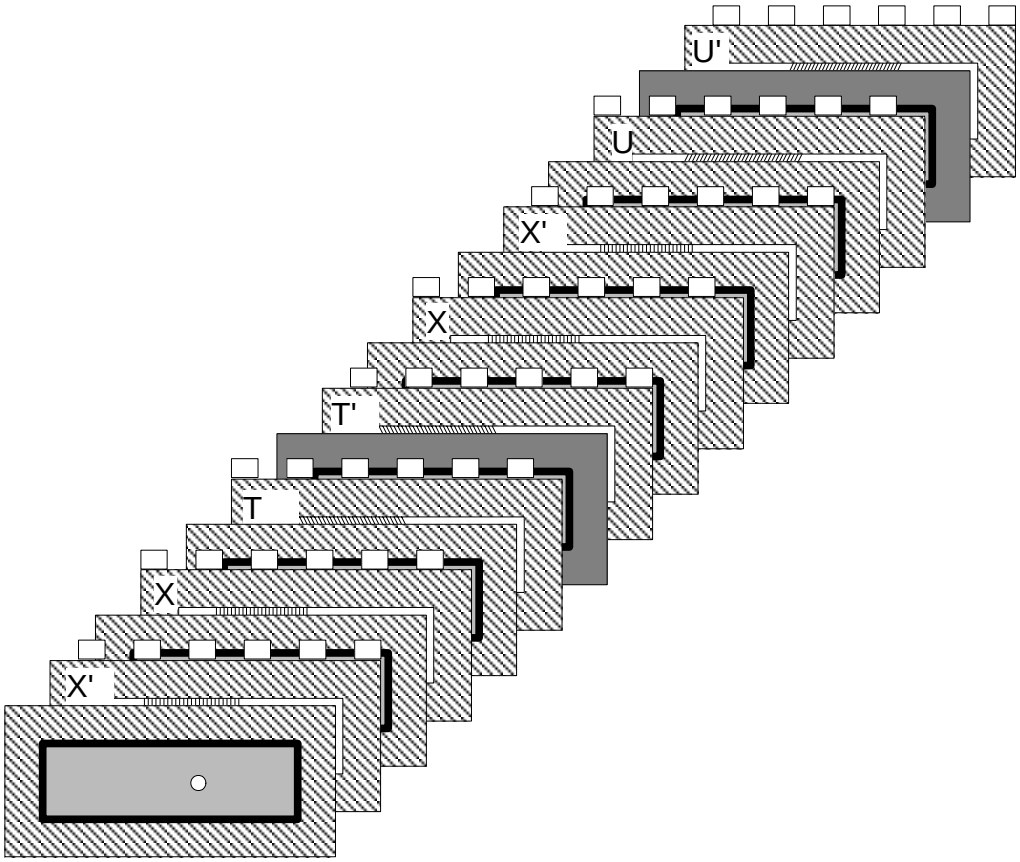
U'
U
X'
X
T'
T
X
X'

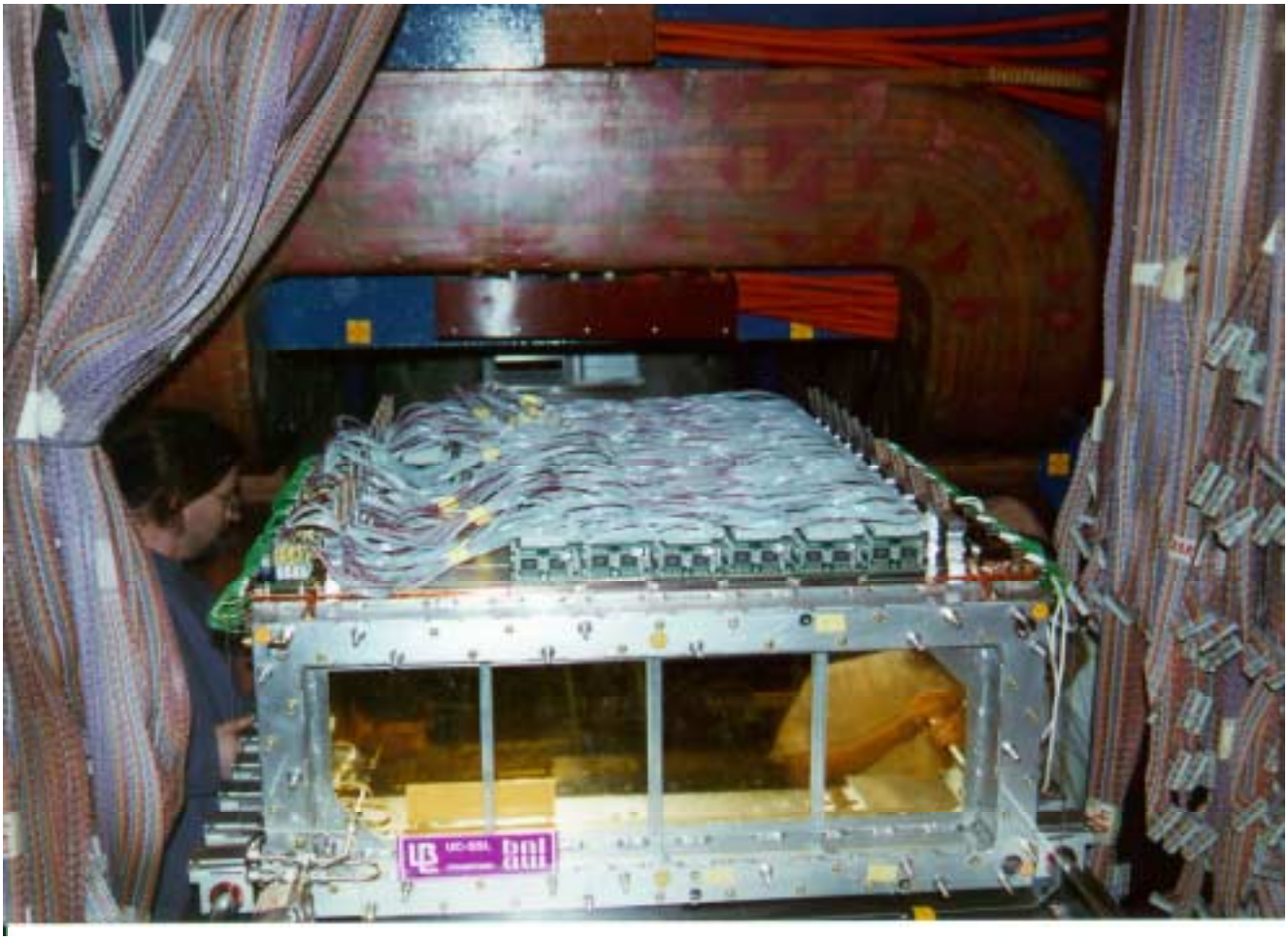

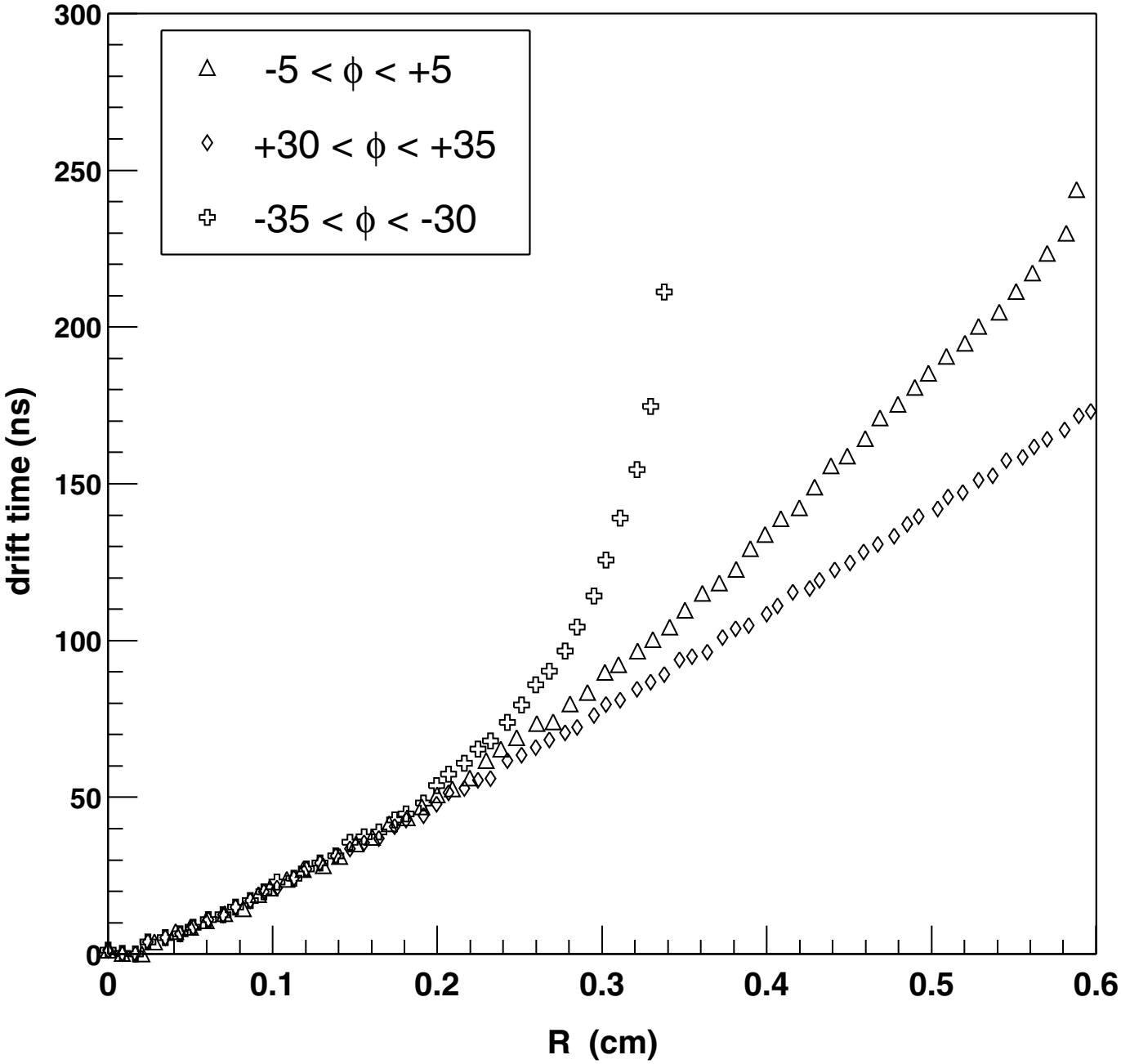
-5 < ϕ < +5
+30 < ϕ < +35
-35 < ϕ < -30
drift time (ns)
R (cm)
0
50
100
150
200
250
300
0
0.1
0.2
0.3
0.4
0.5
0.6

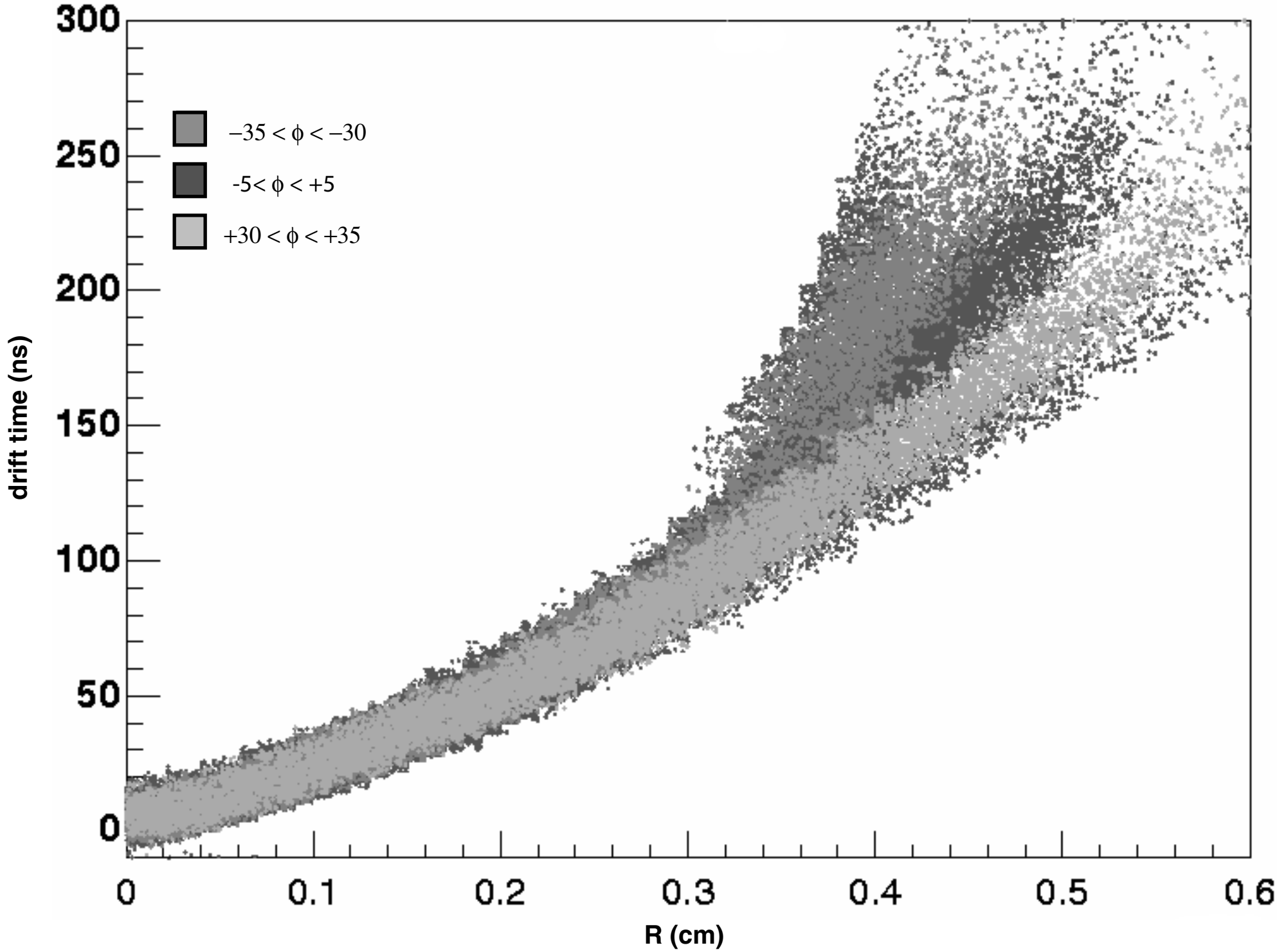
−35 < ϕ < −30
-5< ϕ < +5
+30 < ϕ < +35
drift time (ns)
R (cm)
300
250
200
150
100
50
0
0
0.1
0.2
0.3
0.4
0.5
0.6

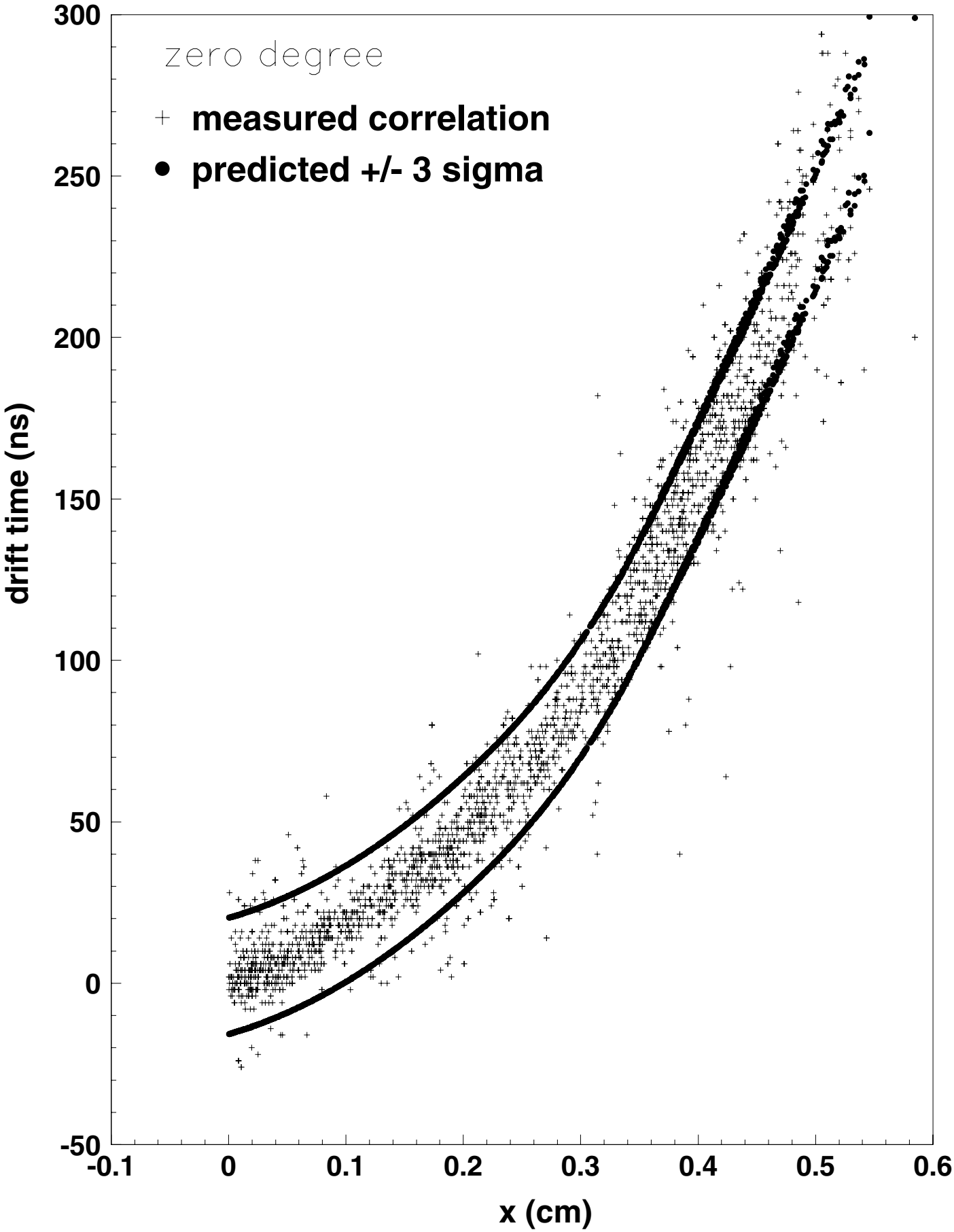
zero degree
measured correlation
predicted +/- 3 sigma
drift time (ns)
x (cm)
300
250
200
150
100
50
0
-50
-0.1
0
0.1
0.2
0.3
0.4
0.5
0.6

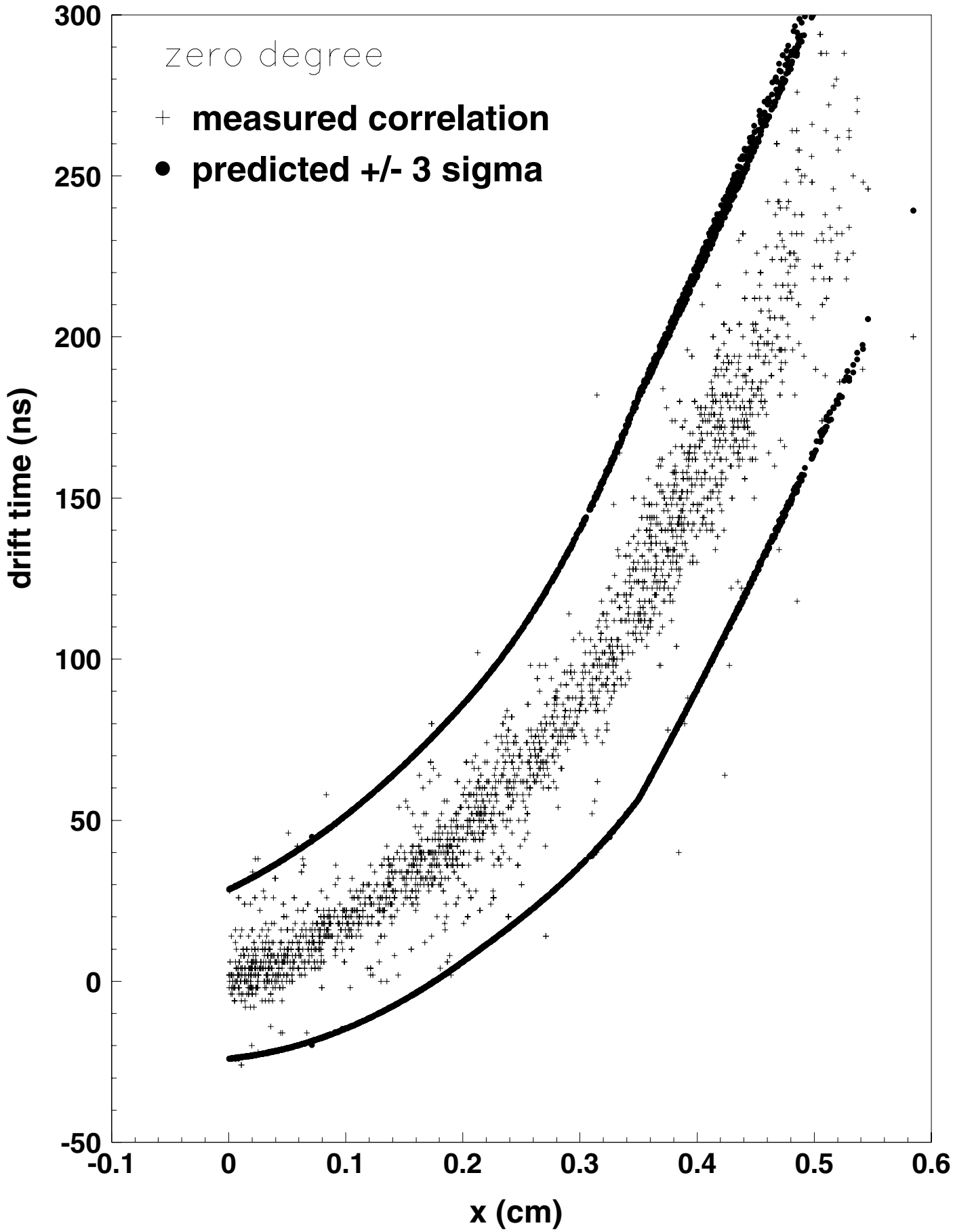
zero degree
measured correlation
predicted +/- 3 sigma
drift time (ns)
x (cm)
300
250
200
150
100
50
0
-50
-0.1
0
0.1
0.2
0.3
0.4
0.5
0.6

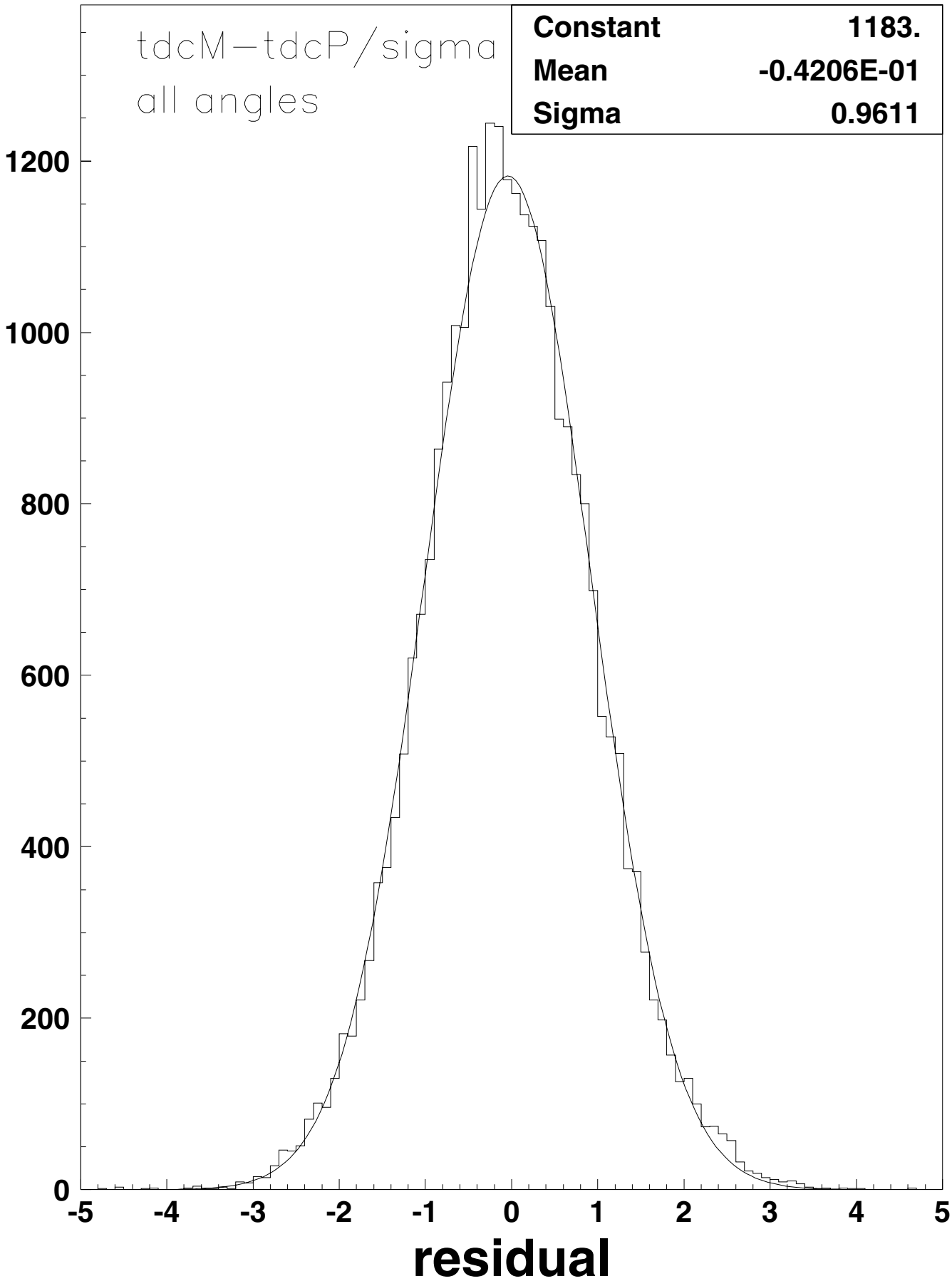
tdcM−tdcP/sigma
all angles
Constant 1183.
Mean -0.4206E-01
Sigma 0.9611
1200
1000
800
600
400
200
0
-5
-4
-3
-2
-1
0
1
2
3
4
5
residual

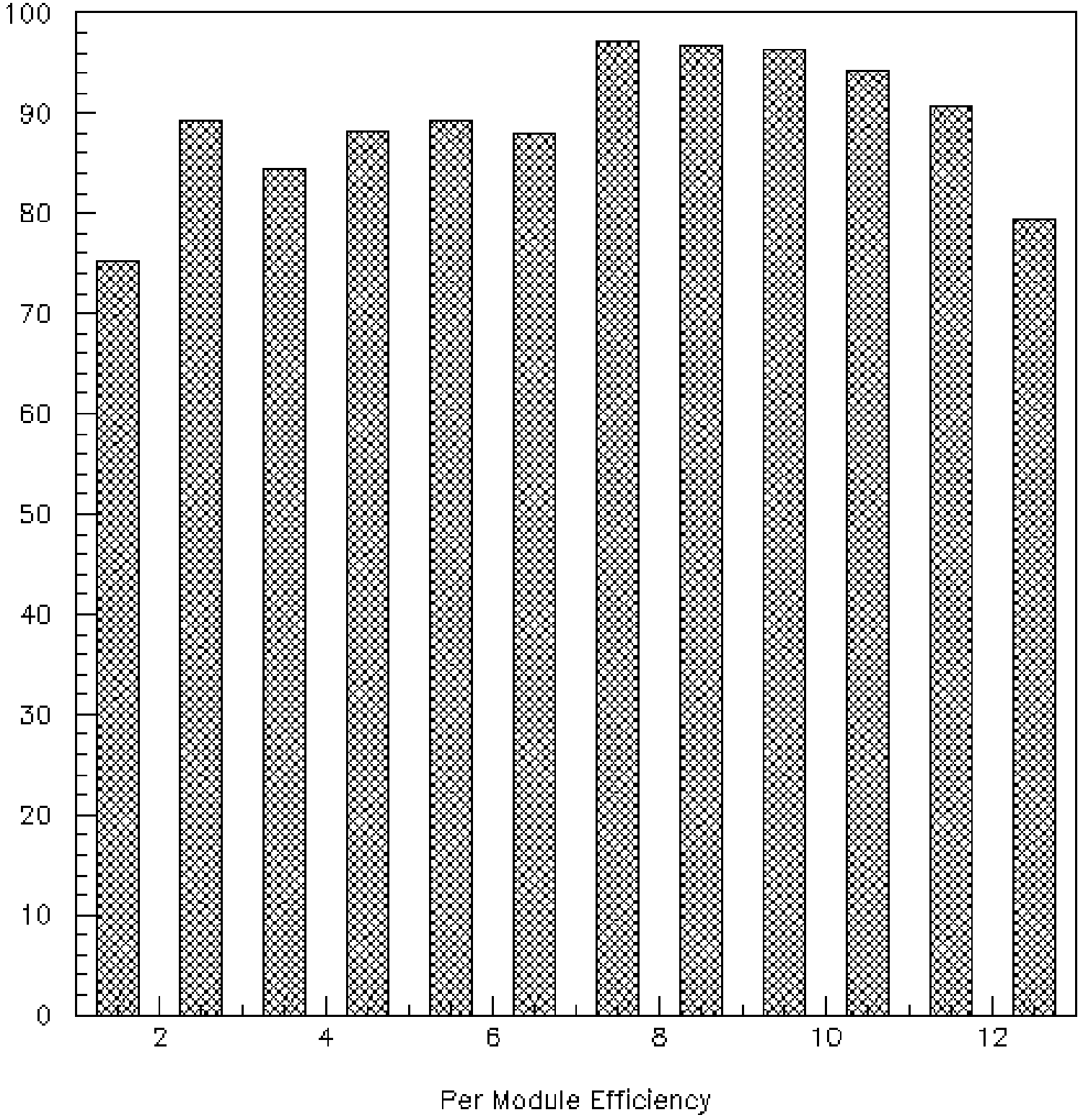
100
90
80
70
60
50
40
30
20
10
0
2
4
6
8
10
12
Per Module Efficiency

Run2885, event63000152
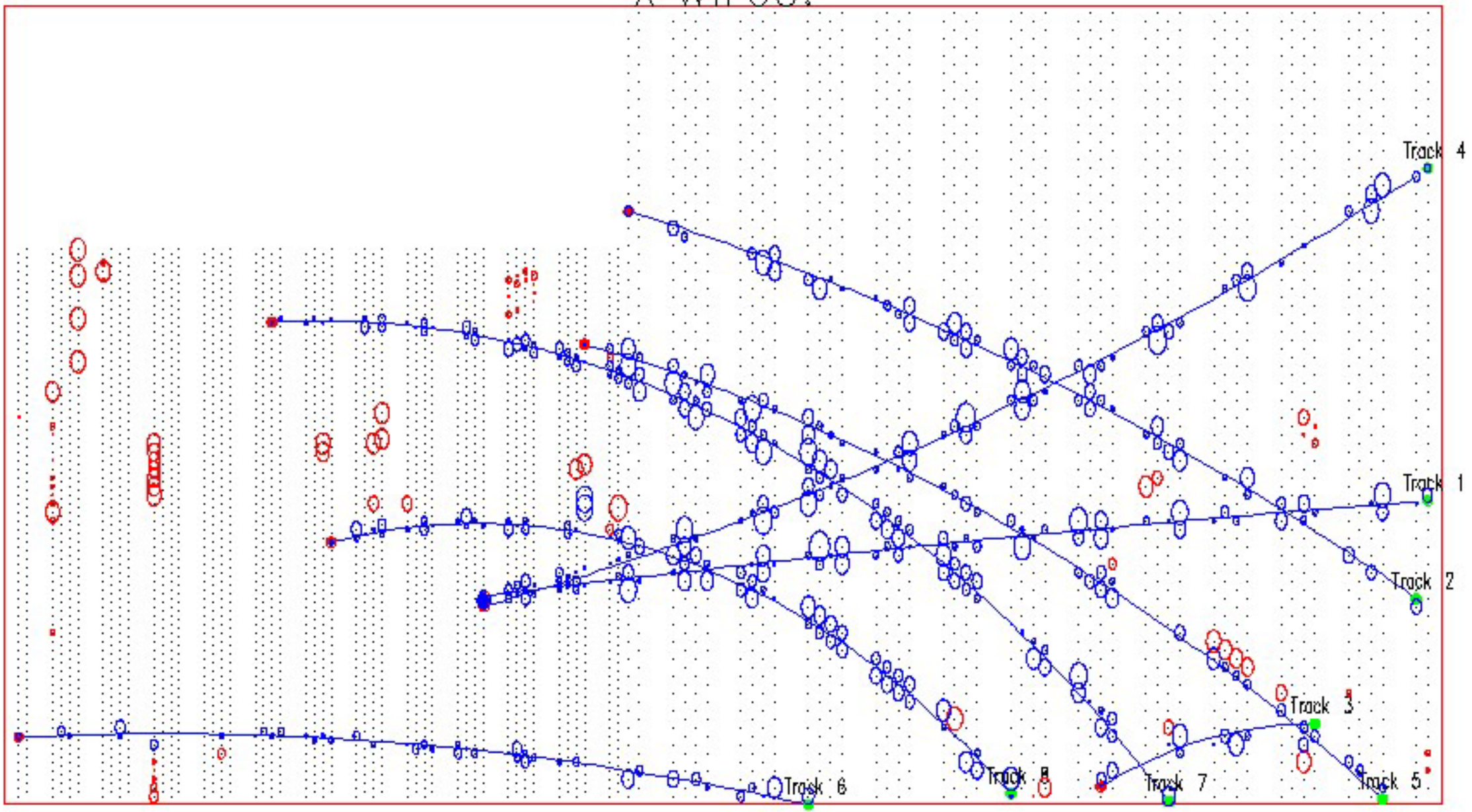
x wires.